Cavitation Inception from Transverse Waves in a Thin Liquid Gap

Julien Rapet,[1,2,*,‡] Pedro A. Quinto-Su,[3] and Claus-Dieter Ohl[2,†]

[1] *Division of Physics and Applied Physics, School of Physical and Mathematical Sciences, Nanyang Technological University, 21 Nanyang Link, Singapore 637371, Singapore*

[2] *Department Soft Matter, Institute for Physics, Otto-von-Guericke-Universität Magdeburg, Universitätsplatz 2, 39016 Magdeburg, Germany*

[3] *Instituto de Ciencias Nucleares, Universidad Nacional Autónoma de México, Apartado Postal 70-543, 04510 Mexico, Cuidad de México, Mexico*

(Received 22 June 2019; revised 25 June 2020; accepted 17 July 2020; published 14 August 2020)

It is well known that dielectric breakdown in a liquid generates cavitation bubbles and shock waves. Here we demonstrate that when the liquid is bounded by two solid glass boundaries (10–20-μm separation), rings of microscopic bubbles can be nucleated around the laser-induced cavitation bubble. While generally acoustic nucleation is achieved with longitudinal waves of sufficient tension, this work demonstrates that acoustic cavitation can also be generated from transverse waves. Our experiments identify three waves originating at the boundaries: the fastest is the bulk wave in the solid, followed by a leaky Rayleigh wave at the liquid-solid contact, which is trailed by a Lamb-type wave. For the latter, the two solid boundaries act as a wave guide and generate intense and short-lived cavitation activity within the gap. Streak photography and high-speed photography reveal the microsecond-duration cavitation-bubble dynamics, and subpicosecond strobe photography visualizes the mechanism of bubble nucleation from the accelerated surface. Simulations coupling the solid mechanics with the acoustics support the experimentally observed mechanisms of transverse-wave-induced cavitation inception.

DOI: 10.1103/PhysRevApplied.14.024041

I. INTRODUCTION

Water exposed to a pulling force may yield and rupture, thereby forming cavitation bubbles. In the presence of nuclei, a few bars of tension suffice [1–4], yet to induce cavitation in small volumes filled with pristine water, much higher forces are necessary. These extreme tensions from negative 100 bar to more than negative 1000 bar can be created with a quasistatic thermodynamic process such as isochoric cooling of the water [5–9] or by focused acoustic waves [10]. Rarefaction waves also form by acoustic diffraction [11,12] or on sound soft reflection of a shock front (e.g., from laser-generated plasmas [13–16]). In general, these laser-generated shock waves are used to compress matter and probe high-density states [17–21] with pressures of several hundred gigapascals. Here we use these pressures generated within the solid and describe a liquid in contact with the propagating transverse wave at the solid-liquid interface. Because of the high surface normal acceleration, the yield strength of water is easily overcome and intense cavitation is generated. This technique thus allows us to probe in a time-resolved manner the yield strength of a liquid in contact with a solid. The advantages are the rather extreme tensile strengths achievable as well as the microscopic access to the liquid while having a rather simple setup. Present state-of-the-art yield-strength measurements need elaborate preparation and are much slower to conduct (see, e.g., Ref. [5]). Our method has some similarity to laser-based ultrasonic techniques [22] where the substrate is irradiated with a short and focused laser pulse to excite surface waves (e.g., for nondestructive testing of the substrate). While laser ultrasonics is done on dry and wet substrates, we add a second substrate to sandwich a 10–20-μm thin water film. Upon laser irradiation of the solids, intense acoustic waves yield the liquid through a special transverse wave, the Lamb-type wave.

The article is organized in the following way: First, we describe the experimental setup that we use to observe the effect. Then, we show our results obtained with different imaging methods (high-speed video, strobe, and streak). In Sec. IV, we use a linear finite-element solver to simulate the waves in the solids, which allows us to identify the three main waves that we observe in the experiment: a bulk wave, a leaky Rayleigh wave, and a Lamb-type wave that nucleates the bubble rings. Next, we discuss the expected deformation of the solids, tensions,

---

[*] julien.rapet@ntu.edu.sg

[†] claus-dieter.ohl@ovgu.de

[‡] Present address: HP-NTU Digital Manufacturing Corporate Lab, 50 Nanyang Avenue, Singapore 639798, Singapore.

and dispersion relations and give other supporting results: from experiments with two thick boundaries and removal of a paint layer due to bubble-ring collapse. Finally, we present our conclusions in Sec. VI.

II. METHODS

A. Experimental setup

The experimental setup to generate and observe the waves and cavitation dynamics is schematized in Fig. 1. It consists of a microfluidic gap, a pulsed laser for generating the bubbles, and an imaging system. Submillimeter bubbles are nucleated with use of a pulsed laser following the classic laser-induced bubble method [23–25]. A microscope objective focuses the laser pulse into the upper surface of the liquid gap and the dynamics is imaged through it, too. Illumination comes from the top, passes through the microscope objective, and is reflected by a half-mirror into one of three different cameras used (see later). A frequency-doubled Nd:YAG laser (Q2-1064 series, pulse duration approximately 10 ns, wavelength 532 nm, and pulse energy between 0.1 and 1 mJ) is expanded with a telescope consisting of two lenses ($f_1 = -30$ mm, $f_2 = 100$ mm) to fill the entrance pupil of the microscope objective. The energy is controlled with a pyroelectric energy sensor (ES145C, Thorlabs). The laser beam passes through the half-mirror and is focused with a 10× microscope objective (UPLFLN10X2, Olympus, NA 0.3). The position of the focus is controlled by adjusting the length of the telescope. By focusing the laser onto the upper microscope slide, the threshold for optical breakdown decreases (specially for low-NA objectives). Dielectric breakdown is produced that induces a rapid rise in pressure from the expanding plasma. We estimate a maximum intensity of 2.6×10^{12} W/cm^2 when focusing on a diffraction-limited spot with a diameter of 2.2 μm and a Rayleigh range of 7.14 μm. The plasma rapidly expands in the opposite direction to the laser beam and the size of the light-emitting plasma region (transverse dimension) obtains a diameter of about 20 μm, while the size in the axial direction is larger and likely covers the thin liquid gap. On expansion of the plasma, a shock wave is emitted into the liquid and an expanding vapor bubble (primary cavitation) is created when the plasma recombines [26]. Besides the expanding cavitation bubble and the shock wave, intense thermoelastic waves [22,27] are emitted from the plasma volume into the glass and back into the liquid. We further observe ablation of the glass [28] due to interaction with the plasma and for sufficiently high energies even cracks.

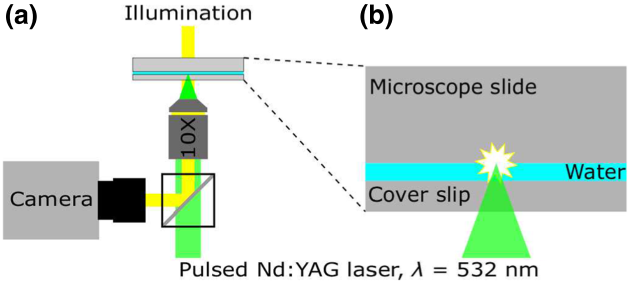

FIG. 1. (a) The experimental setup to simultaneously observe and induce cavitation in a thin liquid gap. (b) Geometry (not to scale) of the liquid gap with the position of the laser focus.

B. Microfluidic gap preparation

The microfluidic gap [Fig. 1(b)] is obtained by sandwiching 15-μm-thick aluminum spacers between a microscope slide (Marienfield soda-lime glass slides, 1 mm) and a coverslip (Carl Roth, thickness no. 1) and is filled with deionized water. The precision of the gap thickness is governed by the surface flatness of the glass plates and the capillary forces. Measurements with micrometer screws and a white-light interferometer determine variations of less than 2 μm of the gap height within the field of view.

C. Imaging

Three different imaging systems are used to observe the complex physical processes occurring in the gap: high-speed video recording, high-resolution strobe imaging with a CCD camera, and streak-camera imaging. For the relatively slow events, a high-speed camera (HPV-2, Shimadzu, Kyoto, Japan) recording up to 1×10^6 frames/s with an exposure time of 250 ns and a resolution of 5.6 μm per pixel is sufficient. The illumination is provided by a single 1-ms-duration camera flash (Auto 3075g, Sunpak, Saitama, Japan) through a condenser lens. The camera is triggered with a delay generator to begin exposure 70 ns before the optical breakdown.

To gain more insight into what happens during the very early moments after the laser is fired, we use stroboscopic subpicosecond-laser-pulse illumination and a higher magnification of 1.1 μm per pixel that enables the visualization of the relevant waves. In this way we are able to resolve the wave propagation and cavitation nucleation by changing the delay between plasma generation and the illumination. The imaging is done with a sensitive CCD camera (PCO.1600, PCO AG, Kelheim, Germany) synchronized to a fast laser strobe (FemtoLux 3 SH, EKSPLA, Vilnius, Lithuania, pulse duration 213 fs at a maximum repetition rate of 50 MHz, wavelength 515 nm). A narrow band-pass filter (FL514.5-3 laser-line filter, Thorlabs) is placed in front of the camera and lets the strobe light pass and reduces the bright continuum emission from the laser plasma. The short exposure time freezes not only the cavitation-bubble dynamics but also the waves traveling in the liquid and solid, increasing the contrast.

The axisymmetry of the bubble structure allows the use of streak imaging to increase the temporal resolution and to image the relevant dynamics in a single shot. For this the streak slit of a streak camera (SC-10, Optronis, Germany) is aligned through the center of the structure; see the dashed lines (SL) in Fig. 3 ($t = 21$ ns). The events are illuminated with a flash lamp (L12745-02, Hamamatsu) with a pulse duration of 2 μs.

III. EXPERIMENTAL RESULTS

A. General dynamics

Figure 2 presents frames extracted from a typical run where the events are recorded with the high-speed camera after focusing of the laser pulse. The intriguing features are the annular rings of cavitation bubbles formed shortly after the laser-induced plasma. The bright spot in the center at $t = 0$ (the time when the laser is triggered) is the location of the focus and is caused by the plasma radiation from the optical breakdown [29]. During the exposure of the first frame lasting 250 ns, a cavitation bubble emerges from the recombined plasma, yet remains hidden in the overexposed image center. The bubble becomes visible after $t = 1$ μs and grows to approximately 540 μm in radius in the next 8 μs. It reaches a maximum radius after approximately 40μs and starts to shrink thereafter. See the Appendix for the video (Video 1) of a similar experiment recorded at 500 000 frames/s and showing the dynamics of the primary cavitation.

We hereafter refer to the central laser-induced bubble as the primary cavitation bubble and refer to the annular rings as secondary cavitation. The formation of these rings is already visible at $t = 0$, yet due to the finite exposure time and their small size, they are captured with their motion blurred. During the time interval of 180 ns between the optical breakdown and the end of the exposure of the $t = 0$ frame, bubbles at a distance as far as $r \approx 560$ μm are observed. We want to address the question of what causes the nucleation of the secondary cavitation bubbles. One would expect a pressure spike rather than a tension wave from optical breakdown in a liquid [26,30,31]. After 1 μs, the cavitation bubbles become prominently visible on concentric rings that have grown to tens of micrometers and populate now the entire frame. The size of some bubbles is sufficiently large to cover the liquid gap, even if the bubbles are nucleated near the glass, where the cavitation threshold is lower. At the same time, an area with a radius of approximately 440 μm around the focus position has been cleared of bubbles. While the primary cavitation bubble expands, the region of secondary cavitation steadily shrinks and disappears, starting from the inner rim until most of the image is cleared of bubbles; see the $t = 8$ μs frame in Fig. 2. Later the secondary cavitation bubbles will rebound and collapse again; see Video 1. The permanent dark spot in the center of each frame is caused by the ablation of the glass.

B. Early dynamics

As observed previously, the phenomenon responsible for the secondary cavitation is incredibly fast and happens within the exposure time of a single frame from the high-speed recording. To better understand what happens during the first frame in Fig. 2 we use stroboscopic subpicosecond imaging as described in Sec. II C. Figure 3 depicts single instants of time from four different experiments. In the first three frames, the secondary cavitation bubbles are nucleated during the exposure time, $t = 21$ ns and $t = 80$ ns, and shortly afterward, $t = 232$ ns, of the first frame in Fig. 2. The outline of the primary cavitation bubble in the center shows some deviation from a cylindrical cross section ($t = 21$ ns) and is surrounded by concentric rings. The outermost ring, labeled B in Fig. 3, is caused by the modulation of the index of refraction in the glass by the fastest wave. The speed $v_B = 5380 \pm 51$ m/s indicates that the outermost ring is a longitudinal bulk wave in the glass spreading spherically. The velocities are obtained from multistrobed images with a 20-ns delay. The averages are obtained from seven runs on the same sample.

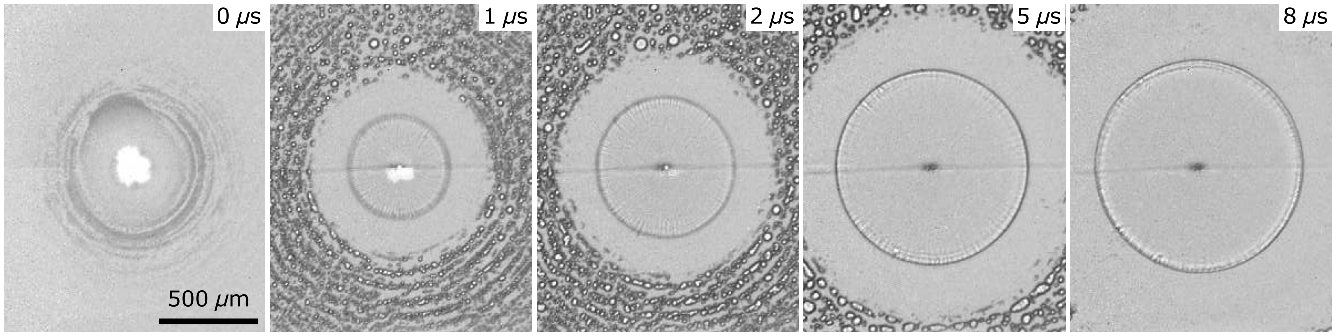

FIG. 2. Cavitation activity within a 20-μm-thick liquid gap following laser-induced dielectric breakdown: selected images from the first 8 μs from one high-speed recording taken at 1×10^6 frames/s with an exposure time of 250 ns. The central bright spot is from the plasma emission.

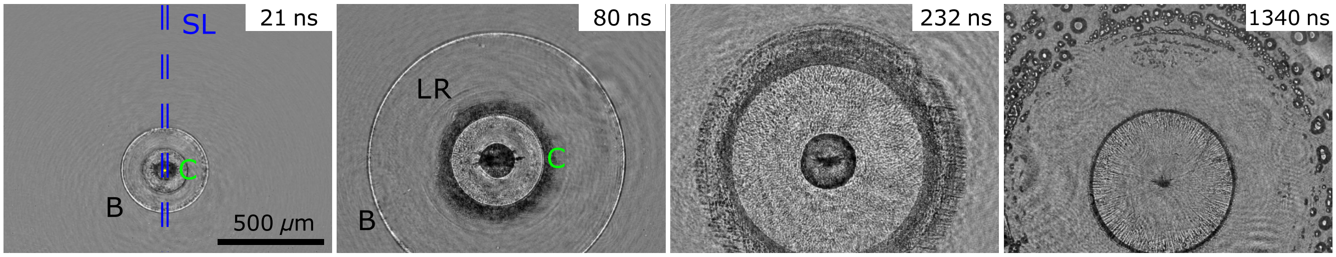

FIG. 3. Stroboscopic and magnified view of the phenomena occurring in the gap. The $t = 21$ ns, $t = 80$ ns, and $t = 232$ ns frames depict the events occurring during the first frame in Fig. 2 and shortly after. The outermost wave is from the bulk wave (B), followed by a leaky Rayleigh wave (LR). The annular ring (C) is the cavitation region propagating outward. The $t = 1340$ ns frame shows how the cavitation bubbles have grown to resemble those in the second frame in Fig. 2. The dashed lines (SL) shows the position of the slit of the streak-camera used to obtain the streak images (Fig. 4).

The bulk wave is followed by what we identify as a leaky Rayleigh wave (LR in Fig. 3) [32] traveling at a prominently slower speed v_{LR} of 3240 ± 36 m/s. Closer to the focus we observe an annular ring of microscopic cavitation bubbles (C in Fig. 3). These bubbles appear to be at the edge or even in front of the laser-induced shock wave in the liquid, which is hard to observe because there is another wave that propagates at a similar speed that nucleates the bubbles. Later we identify it as a Lamb wave. The region between this ring and the primary cavitation bubbles is filled with a patterned region, which under close inspection is composed of many overlapping spherical waves. These waves are emitted from bubbles that collapse at the inner rim of the ring (C in Fig. 3). Shortly after at $t = 232$ ns (from a different run) the diameter of the ring increases (i.e., it propagates outward while some of the bubbles that were imaged at an earlier time have already collapsed). The velocity of the inner rim (where the bubbles are nucleated first) of the annular cavitation ring $v = 1510 \pm 82$ m/s, which is on the order of the speed of sound in the liquid and similar to the speed of a laser-induced shock wave in the liquid. The acoustic waves emitted from ring C toward the primary cavitation bubble already indicate that the cavitation bubbles undergo violent collapses. The last frame, at $t = 1340$ ns, shows how the secondary cavitation bubbles have grown to resemble those in the second frame in Fig. 2. We do not observe luminescence or the emission of shock waves upon collapse of the primary cavitation bubble. This is an effect of the quasi-two-dimensional geometry of the liquid that dampens the collapse [33].

While we reveal the formation and collapse of cavitation within a gap, the question remains as to what induces the necessary tensile stress for cavitation nucleation. We take advantage of the axisymmetric geometry of our system and use streak imaging (see Sec. II C) to increase the temporal resolution and capture the dynamics of the first instants. A typical streak image is presented in Fig. 4 as an r-t diagram. The vertical axis spans a distance of 1.2 mm, and the time on the horizontal axis ranges from 0 to 1500 ns, which covers approximately the first two frames in Fig. 2. The bright spot at $r = 0$ is from the plasma (luminescence spans about 100 ns), out of which the primary cavitation bubble expands. Below the primary bubble we observe horizontal stripes (secondary cavitation). Their length increases quickly (at a rate of about 1700 m/s) with time, and after about 300 ns the nucleated bubbles remain for the duration of the streak recording, while the bubbles that are nucleated before collapse within a few-hundred nanoseconds. The rate at which the horizontal stripes appear is the phase velocity of the wave generating the cavitation region. Here we measure a maximum initial velocity of 1712 ± 107 m/s (11 events), similar to the expansion velocity obtained with the single-frame camera as shown in Fig. 3. This velocity is similar to the speed of a regular shock wave in the liquid and suggests that the bubble rings are nucleated from the rarefaction part of an acoustic wave. However, we are not aware of cavitation inception being reported from a simple laser-induced breakdown in a pure liquid (i.e., the shock wave emitted in the liquid having sufficient tension). As the geometry is very confined, waves in the solid may be responsible

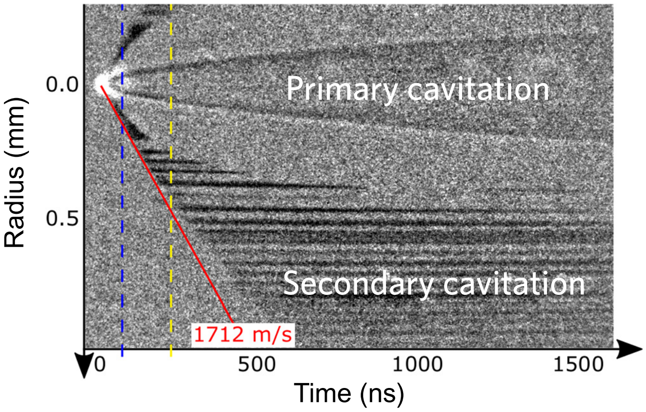

FIG. 4. Streak-camera image with a height of 1.2 mm and a width of 1500 ns. The bright spot is the plasma, followed by the primary bubble and secondary bubbles.

for the tension. However, in the experiments we do not observe expansion of bubbles after the passage of the bulk (B) wave and very rarely after the passage of the leaky Rayleigh wave (LR). Thus, the wave that is creating the rings of secondary bubbles is a different wave, which we try to identify through comparison with simulations.

IV. COUPLED SOLID-LIQUID WAVES IN A THIN GAP

A. Finite-element simulations

Normally, optical breakdown in a liquid results in the emission of a shock wave and the generation of a cavitation bubble. The experimental results indicate that the secondary cavitation bubbles are nucleated by a wave propagating at the speed of the laser-induced shock wave but with sufficient tension to rupture the liquid. To understand how the presence of the two glass boundaries allows such a wave to exist, we use a simplified model that considers only exciting waves in the solids, which later leak into the liquid. While the laser is focused on the upper microscope slide, the plasma expands into the liquid gap and onto the lower glass slide. We model this in a first approximation by symmetric loading of both glass boundaries. The model yields reasonable results that are consistent with our measurements and the geometry of the bubble rings. We do not consider loading the liquid because we know that the laser-induced shock wave propagates at a similar speed as the wave originating in the solid that nucleates the bubbles. We want to isolate the effect of the waves induced in the solids. Also, the primary cavitation bubble is not considered, as the events that we report are much faster than the primary-bubble dynamics.

The axisymmetric problem is solved with COMSOL MULTIPHYSICS. The domain (see Fig. 5) consists of two layers of linear elastic material (Solid Mechanics, *solid*, elastic modulus $E = 63$ GPa, Poisson ratio $\nu = 0.2$) sandwiching a layer of a linear acoustic material (Pressure acoustics, Transient, *actd*). The coupling between the transverse waves in the elastic solid described by the deformation field $\mathbf{u}(\mathbf{x}, t)$ of the glass with the acoustic pressure $p(\mathbf{x}, t)$ in the liquid gap is done through the linearized Euler equation:

$$-\frac{1}{\rho_f}\nabla p = \frac{\partial^2 \mathbf{u}}{\partial t^2}, \tag{1}$$

where ρ_f is the density of the fluid. The fluid pressure is coupled into the solid mechanics as a normal force. The loading of the solid is modeled with a spatial and temporal localized pressure acting at the liquid-solid interface. This pressure acts normal on the solid within a region of radius $R = 10$ μm and for a duration of the laser pulse Δt of 10 ns. This pressure from the plasma during the dielectric breakdown of the solid is abstracted as

$$p(r,t) = \begin{cases} \hat{P}\cos\left(\frac{\pi r}{2R}\right)^2 \sin\left(\frac{\pi t}{\Delta t}\right)^2 & \text{for } 0 < t \leq \Delta t, \\ 0 & \text{otherwise.} \end{cases} \tag{2}$$

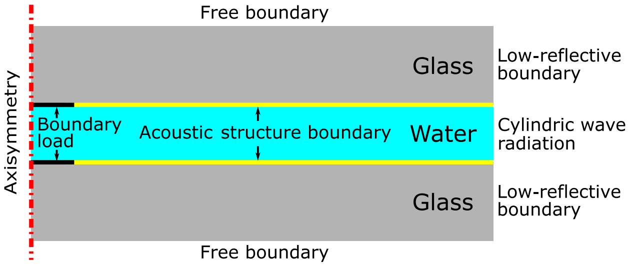

FIG. 5. Geometry of the simulation domain with the boundary conditions for solving the coupled acoustic-elastic wave problem.

The pressure amplitude $\hat{P} = 10$ GPa is motivated by Ref. [27]. While we have no measurement of our own to justify this value, the magnitude is a reasonable choice. In particular, a similar pressure (6 GPa) was found to give good agreement when comparing the shock-wave emission and expansion of a bubble in a microfluidic channel [13] with numerical simulations. In that experiment the pulse duration is similar but the wavelength is larger: 1064 nm, resulting in higher energy thresholds for optical breakdown (compared with 532 nm). Another experiment [14], where the laser parameters (pulse duration and 532-nm wavelength) are essentially identical to those in this experiment, reported optical breakdown in water with energies on the order of 75 μJ. The resulting dynamics were simulated with initial pressures of 2 GPa. Here the laser pulses have about 10 times more energy, and hence an initial pressure amplitude of 10 GPa is reasonable. Choosing a different amplitude $\hat{P}$ will scale the reported pressures but would not change the qualitative picture because all equations and boundary conditions involved are linear.

B. Surface-wave generation in a thin gap

Snapshots of the solution from an axisymmetric simulation with a 20-μm-thick water layer are depicted in Fig. 6(a). The initial condition is the pressure $p_{\rm pl} = 10$ GPa [13,27] acting for 10 ns on the solid boundaries in a circular region of $0 \leq r \leq 10$ μm to simulate the plasma pressure from the laser-induced breakdown. Positive pressures are depicted in red and tension is depicted in blue. The snapshots at times $t = 20, 29, 59$, and 89 ns reveal the formation of a rather-complex sequence of waves originating from the central region. At $t = 20$ ns, which is 10 ns after excitation, the rightmost wave, with a small amplitude, is caused by the longitudinal bulk wave in the solid that is leaking into the liquid [B in Fig. 6(a)]. This wave is followed by

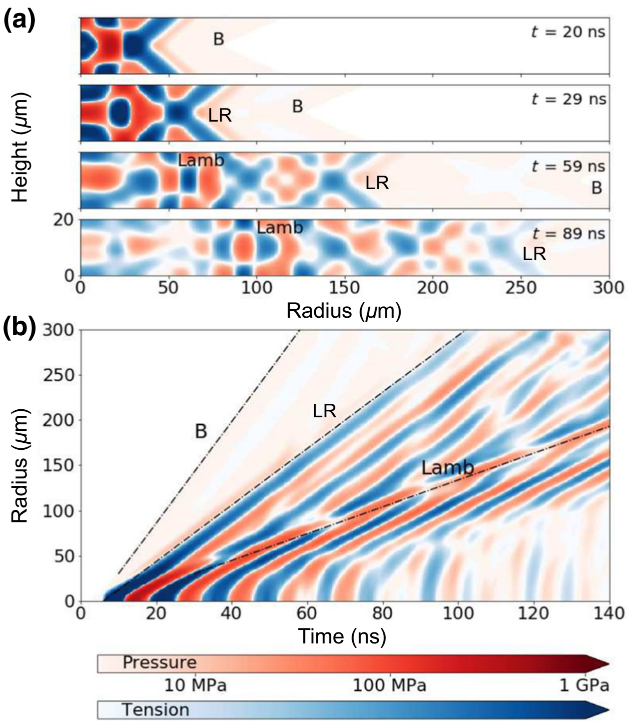

FIG. 6. Simulations of acoustic wave propagation in a 20-μm-thick water-filled gap. (a) Side view of the waves with tension (blue) and pressure (red) for four instances of time. (b) r-t diagram of the pressure at the center of the channel. The three distinct waves are the leaking longitudinal bulk wave (B), the leaky Rayleigh wave (LR), and the Lamb wave. See the Appendix for the video (Video 2) of the simulation.

the leaky Rayleigh wave [LR in Fig. 6(a)] creating Mach cones in the liquid and is starting to separate from the central region at $t = 29$ ns. Experimentally, we do not observe bubble nucleation at the position of the leaky Rayleigh wave, probably because the most-negative pressures are reached in the center of the channel and not at the glass boundaries, where the threshold for nucleation is much lower. At $t = 59$ ns, a third wave can be distinguished behind the leaky Rayleigh wave; it results from the reflections of waves between the glass boundaries. This wave with negative pressure is followed by waves that alternate between positive and negative pressures. It creates a symmetric deformation on the glass boundary, while traveling at a much lower velocity than the leaky Rayleigh wave. The separation of this symmetric wave traveling with an acoustic velocity in the liquid from the leaky Rayleigh wave is clearly visible at $t = 89$ ns. Our observations suggest that bubbles are nucleated in the vicinity of this wave. Figure 6(a) shows that this wave is bounded by tensions that should nucleate the bubbles at the surface of the glass (most-negative pressures at the surfaces). Then the bubbles will expand to a few microns, essentially filling the liquid gap.

These three waves are also visible in the r-t diagram in Fig. 6(b), where the pressure in the center of the gap ($z = 10\ \mu$m) is plotted as a function of r and t. The first rather weak wave [B in Fig. 6(b)] is caused by the driving of the liquid by the bulk wave traveling in the solid at speed $v_B = \sqrt{E(1-\nu)/(\rho(1+\nu)(1-2\nu))} = 5602$ m/s and leaking into the liquid. It is followed by a leaky Rayleigh wave [LR in Fig. 6(b)] traveling at $v_{\mathrm{LR}} = \sqrt{E/(2\rho(1+\nu)}(0.862 + 1.14\nu)/(1+\nu) = 3116$ m/s radiating into the liquid gap as a Mach cone. The third wave has a velocity close to the speed of sound in water and is excited by the bending of the boundaries of the thin gap forming a symmetric Lamb mode. Notice that the structure of the pressure fields for a given radius is consistent with the bubble rings (Fig. 2) that appear to be separated. This is explained by the alternating positive and negative pressures for a given radius as time increases.

C. Gap deformation from Lamb-type waves

We present some details on surface waves from the finite-element simulations. Figure 7 depicts the deformation of the gap and the resulting pressure in the center of the 20-μm-thick gap. Both curves are recorded at $r = 130\ \mu$m from the center. The pressure is plotted as a solid line and the change in the gap width is plotted as a dashed line. The timing starts approximately at the expected arrival time ($t \approx 90$ ns) of a wave traveling with the speed of sound. After initial transient oscillations we see a nearly harmonic oscillation pattern starting from $t > 105$ ns. It reaches a minimum pressure of 0.5 kbar and oscillates with $f_l = 83$ MHz and has a wavelength of 18 μm. The gap height varies by approximately 40 nm, from which we can estimate a typical surface normal velocity $u_\perp$ of $\hat{z}2\pi f_g \approx 10$ m/s and acceleration $a_\perp$ of $\hat{z}(2\pi f_l)^2 \approx 5.4 \times 10^9$ m/s^2, where $\hat{z} = 10$ nm is the vertical amplitude of the surface.

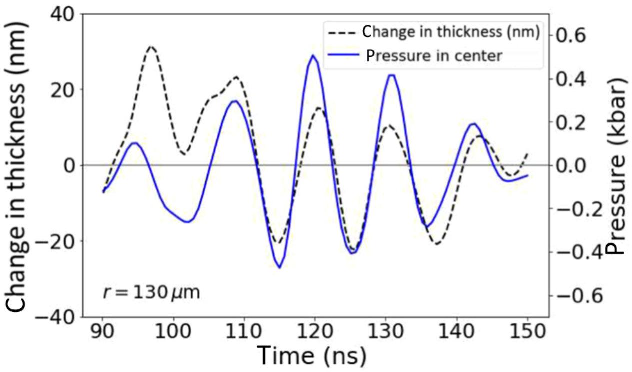

FIG. 7. Pressure in the center of the gap (solid line) and change of gap thickness (dashed line) during the propagation of the Lamb wave.

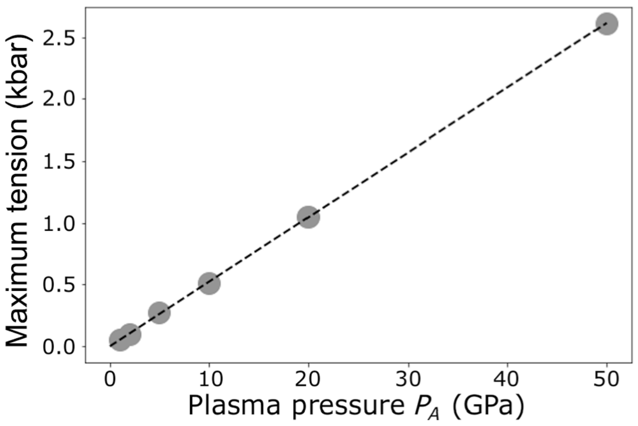

FIG. 8. Maximum tension generated by the Lamb wave as a function of the plasma pressure.

D. Tension in the gap

The maximum attainable tension is a strong function of the initial pressure (i.e., the plasma pressure of the laser-induced breakdown). While we do not model this process, we can test the effect a larger and a smaller pressure would have on the tension created during the passage of the Lamb wave. Figure 8 shows that the tension in the liquid is a linear function of the plasma pressure. The fit gives a slope of $T = 5.23 \times 10^{-3}\ P_A$. This relation is expected for the linear elastic solid and linear acoustic model used in the simulations. Also the model predicts that the homogeneous cavitation threshold of 1.26 kbar [34] will be reached at a driving pressure P_A of 24 GPa, which is smaller than our driving pressure of 10 GPa, supporting the idea of bubbles nucleated close to the surface.

V. DISCUSSION

A. Wave generation in thin liquid gaps

Surface waves generated from a continuous and transient point load on a boundary between infinitely extended solid and liquid domains propagating either supersonically or subsonically with respect to the speed of sound in the liquid. The supersonic wave is termed the “leaky Rayleigh wave” as it radiates energy into the liquid and the subsonic wave is termed the “Scholte wave.” While analytic solutions for transient excitation exist for both waves [32,35], only recently did Doinikov *et al.* [36] obtain solutions for surface waves in a thin liquid gap. Their derived dispersion relation recovers in the limit of zero mass loading of the fluid the Rayleigh waves and recovers the Scholte waves in the limit of high frequencies or an infinite large gap. For thin gaps, however, the dispersion relation provides a new solution; namely, a Lamb wave, which is typically observed in thin elastic solids that are bounded by a vacuum [37,38]. In contrast to conventional Lamb waves in solids, here the Lamb-type waves are expanding and compressing the liquid. In the original study [36], the thin liquid gap was sandwiched by two layers of soft rubber and the pointlike loading was achieved with a bubble undergoing stable volume oscillations. This symmetric excitation leads to symmetric Lamb waves. In our present experiment we cannot rule out antisymmetric waves, and therefore we extended the derivation of Doinikov *et al.* [36] to antisymmetric modes. Also, while the theory is unchanged, the application region is largely different in the present experiment. First, the elastic modulus of the glass is many orders of magnitude higher than that of soft rubber, and also our excitation frequency is considerably higher as compared with that for the acoustically driven bubble at a few tens of kilohertz. We can estimate the driving frequency with the round-trip time of the acoustic wave in the gap; that is, $f = c/2h \approx 40$ MHz, where $c \approx 1500$ m/s is the speed of sound and h is the gap height of approximately 20 μm.

A sketch of the geometry solved for is provided in Fig. 9. The system is axisymmetric with its center, $r = 0$ and $z = 0$, located in the liquid in the center of the channel. $z = h/2$ is the upper boundary between the liquid and the solid, and $z = -h/2$ is the lower boundary. The indices H_0 and H_1 indicate that the Hankel transforms of order 0 and 1 are used. While for the calculations of the deformation the inverse Hankel transform is needed, we do not need this additional complexity to calculate the wave velocity as a function of ω and h.

The displacements of the upper wall ($j = 1$) and the lower wall ($j = 2$) are in the radial and vertical directions u_{jr} and u_{jz}, respectively. Φ_j, Φ_{fj}, and Ψ_j are scalar functions of the wave number k and are determined by the boundary conditions. The boundary conditions for the symmetric case (upper sign) [36] and for the antisymmetric

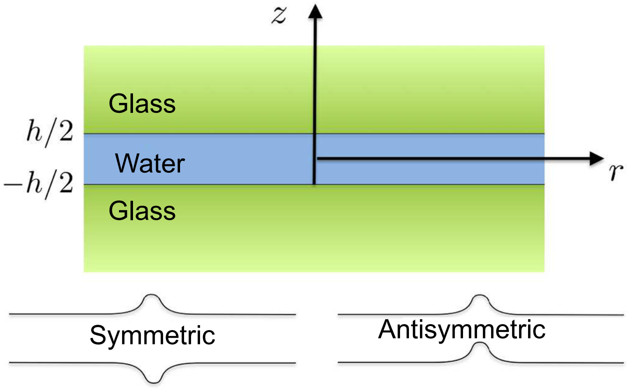

FIG. 9. The glass-solid-glass geometry. Axisymmetry is assumed. A symmetric Lamb mode and an antisymmetric Lamb mode of the two glass plates are depicted at the bottom.

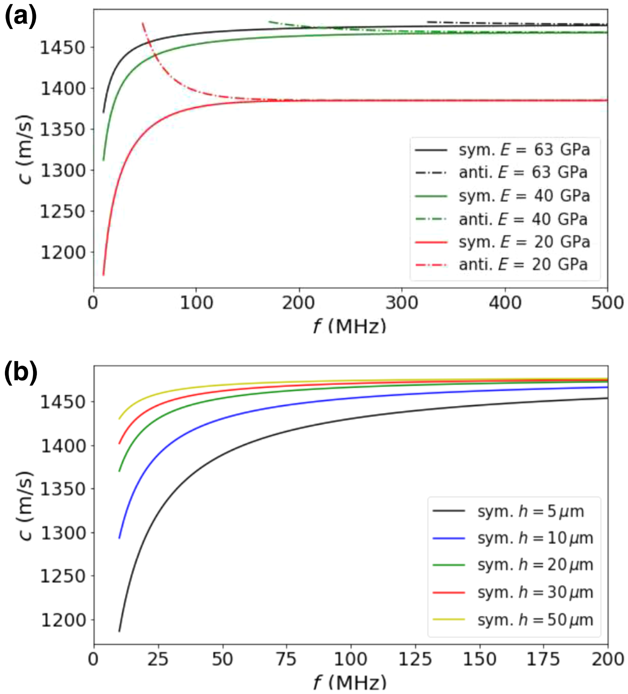

FIG. 10. Dispersion curve as a function of the elastic modulus (a) and as a function of the gap height (b) (anti., antisymmetric mode; sym., symmetric mode).

case (lower sign) are as follows:

$$u_{1r}^{H_1}(z = h/2) = u_{2r}^{H_1}(z = -h/2), \tag{3}$$

$$u_{1z}^{H_0}(z = h/2) = \mp u_{2z}^{H_0}(z = -h/2), \tag{4}$$

$$\Phi_2(k) = \pm\Phi_1(k), \tag{5}$$

$$\Phi_{f\,2}(k) = \pm\Phi_{f\,1}(k) = \pm\Phi_f(k), \tag{6}$$

$$\Psi_2(k) = \mp\Psi_1(k). \tag{7}$$

We can then write Eqs. (2.41)–(2.46) from Doinikov *et al.* [36] with three equations for Φ_1, Ψ_1, and ϕ_f as the unknowns:

$$q_l\Phi_1 - k\Psi_1 + q_f\left(1 \mp e^{-q_f h}\right)\phi_f = 0, \tag{8}$$

$$2kq_l\Phi_1 - \left(2k^2 - k_f{}^2\right)\Psi_1 = 0, \tag{9}$$

$$\left(2k^2 - k_t^2\right)\Phi_1 - 2kq_l\Psi_1 + \frac{\rho_f\omega^2}{\mu}\left(1 \pm e^{-q_f h}\right)\phi_f = -\frac{Q}{2\pi\mu}, \tag{10}$$

where $q_l^2 = k^2 - k_l^2$, with k_l being the wave number for the longitudinal wave, k_t is the wave number for the transverse wave, $q_f^2 = k^2 - k_f^2$, with k_f being the wave number for the sound field in the fluid. ω is the angular frequency, ρ_f is the fluid density, μ is the shear modulus of the solid, and Q is the magnitude of the point loading. Again the symmetric case uses the upper sign and the antisymmetric case uses the lower sign.

Using Cramer's rule, we can solve these inhomogeneous linear systems of equations. Solution of the dispersion equation $D(k) = 0$, where $D(k)$ is the determinant of the above equations, results in the dispersion curves $c(\omega)$ for the symmetric and antisymmetric Lamb waves:

$$D(k) = \left(2k^2 - k_t^2\right)^2 - 4k^2 q_l q_t + \frac{\rho_f\, k_t{}^4 q_l}{\rho_s q_f}\,\frac{1 \pm e^{-q_f h}}{1 \mp e^{-q_f h}}, \tag{11}$$

where ρ_s is the density of the solid.

Next we present the roots of Eq. (11), which are the Lamb type of symmetric and antisymmetric waves. Figure 10(a) demonstrates this dispersion relation $c(f)$, where c is the phase velocity of the wave and $f = 2\pi\omega$ is the frequency for the symmetric (solid lines) and antisymmetric (dashed lines) waves. The three pairs of curves are for selected elastic moduli $E = 63, 40$, and 20 GPa and gap height $h = 20$ μm. The other parameters are $\rho_s = 2230$ kg/m^3, $\rho_f = 998$ kg/m^3, and the speed of sound in the liquid $c_f = 1481$ m/s. In the limit of $f =\rightarrow \infty$ the wave velocity approaches to Scholte-wave velocity (i.e., $h \rightarrow \infty$ for the symmetric and antisymmetric waves). The speed of sound in the liquid c_f is the upper limit of the Lamb-wave velocity. We find that the symmetric wave can propagate in the expected frequency range of 40 MHz for the elastic modulus of glass $E = 63$ GPa, while the antisymmetric wave may propagate only for a smaller modulus.

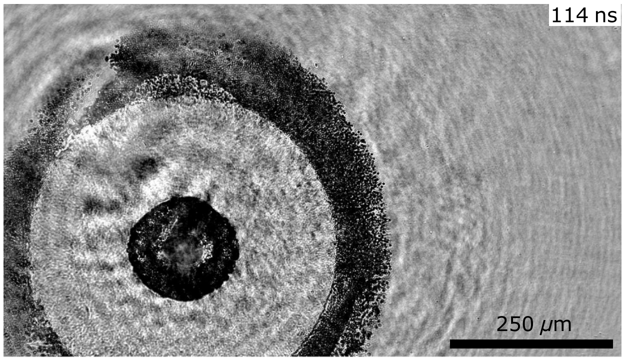

FIG. 11. Stroboscopic and magnified view of the cavitation activity within a 20-μm-thick liquid gap bounded by two thick glass plates (1 mm).

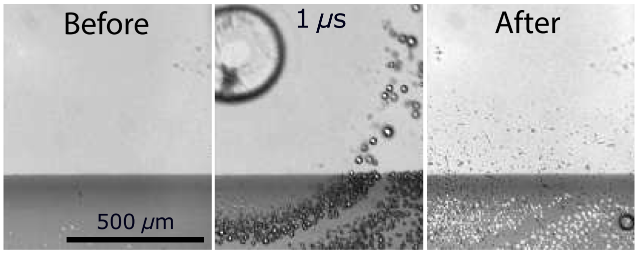

FIG. 12. Demonstration of cavitation erosion: at the locations of cavitation activity ($t = 1$ μs) bright spots appear (see the “after” image), indicating the removal of the thin film from a waterproof marker.

The second dependency of the dispersion curve is the gap height; see Fig. 10(b).

Lamb waves in solids have also been reported to create acoustic waves [39]. To rule out that the Lamb wave in the thin coverslip is responsible for acoustic waves radiated into the liquid gap, we vary the thickness to a 1-mm glass plate. We observe again a similar cavitation pattern; see Fig. 11. Thus, a Lamb wave in the solid can be ruled out.

B. Removal of a paint layer

The violent character of the collapse of the secondary cavitation is further confirmed in an experiment where a thin paint layer is added on the glass plate (top). Snapshots of the experiment are presented in Fig. 12, and the full video is available in the Appendix (Video 3). There we observe that the smooth dark stripe on the left of the frame before the cavitation activity (left frame) is pictured with the bubbles present at $t = 1$ μs and long after ($t = 210$ s) the collapse in the right frame in Fig. 12. The latter image reveals many bright spots at the locations where bubbles have appeared. This pattern resembles the erosion patterns found on foils subjected to acoustic cavitation [40]. The collapse of the secondary cavitation bubbles is sufficiently intense to remove locally the film from the surface. Some of the collapses are induced by the other positive-pressure waves that eventually reach the bubbles or just regular Rayleigh collapse. We do not expect that the collapse is connected with the dynamics of the primary cavitation bubble or the induced flow as it expands, as the dynamics of the main bubble is much slower than the times involved in this experiment.

VI. CONCLUSION

In summary, we demonstrate that cavitation in liquids can be induced from intense transverse waves at the liquid-solid surfaces of a thin liquid gap. Most prominently, a Lamb-type wave nucleates cavitation bubbles of diameter up to approximately 10 μm that last for several microseconds. Their collapses are sufficiently strong to erode the surface and could open interesting perspectives for treatments of metallic surfaces by cavitation peening [41] or for surface cleaning [42,43] and biofilm removal [44]. These transverse waves can be nucleated only if the initial pressure disturbance is sufficiently strong and confined. For the present experiments, the plasma pressure from the laser-induced breakdown generates a pressure of several gigapascals on an area with a diameter of a few micrometers. The tension created from the transverse waves provides a method to nucleate even nanoscopic pockets of gases and test for cavitation nuclei and their stability on substrates. Furthermore, the precise timing of the cavitation event with respect to the nanosecond-duration laser pulse may offer an alternative route to explore sonochemistry from cavitation-bubble collapse spatially and temporally resolved [45]. The results of these experiments are important for many applications in microfluidic that use optical breakdown to pump [46] and mix [47] liquids; switch [48] microscopic objects; porate [49], stretch [50] and lyse [51] biological cells. In general, this work will help set design limits for microfluidic systems that are actuated by large impulsive forces in order to enhance or hinder the effect that we are reporting. Finally, the present simulations are limited to a linear response of the solid. They should be expanded to account for finite-amplitude effects and eventually coupled to a multiphase-flow solver that can account for cavitation nucleation.

ACKNOWLEDGMENTS

The work was supported by the Joint Research Programme of the National Natural Science Foundation of China (Grant No. 11861131005) and the Deutsche Forschungsgemeinschaft (Grant No. OH 75/3-1). P.A.Q.-S. acknowledges support from CONACYT (projects CB-253706 and LN-299057) and Dirección General Asuntos del Personal Académico, Universidad Nacional Autónoma de México (project IN107719).

APPENDIX: VIDEOS

Here, we present the full-length video of the numerical simulation along with the recordings of two secondary cavitation experiments. One recorded at 500 000 frames/s shows the long-term dynamics and the other one shows the removal of a paint layer.

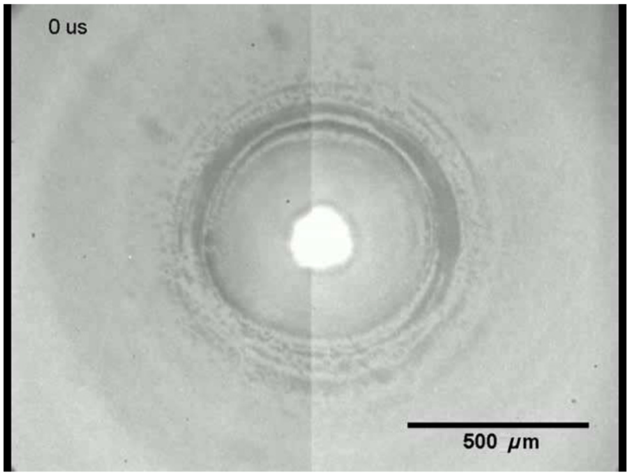

VIDEO 1. Recording of an experiment similar to the one presented in Fig. 2. The recording speed is 500 000 frames/s with an exposure time of 250 ns and a resolution of 5.6 μm per pixel. With the slower frame rate we capture the dynamics of the primary cavitation from nucleation to its first collapse. The bubble is created at $t = 0$. The bright spot due to the plasma indicates the position of the focus. Secondary cavitation is already visible as a darker gray-ring cloud of very fine bubbles around the plasma spot. These bubbles grow to tens of micrometers in size and disappear almost completely within 8 μs, before rebounding. The primary cavitation bubble is initially hidden by the bright light from the plasma ($t = 0$). The bubble becomes visible after $t = 2$ μs. It expands rapidly during the first 8 μs, maintaining a quasicylindrical shape before slowing down and deforming. It has a maximum expansion around $t = 34$ μs, then starts shrinking, and reaches a minimum volume at $t = 128$ μs. We do not observe luminescence or the emission of shock waves upon collapse of the primary cavitation bubble. This is an effect of the quasi-two-dimensional geometry of the liquid that dampens the collapse [33].

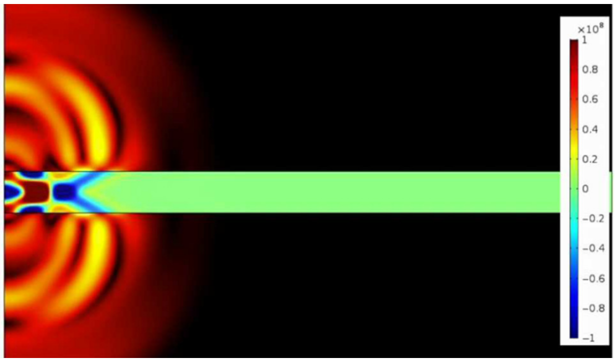

VIDEO 2. Results of the simulation described in Sec. IV and that covers a duration of 150 ns and the region shown in Fig. 5. The acoustic pressure in the 20-μm-thick gap is plotted with red colors (positive) and blue colors (negative) on a fixed and linear color scale, shown to the right. The pressure range is ±100 MPa. Clearly the leaky Rayleigh wave and the Lamb wave are visible. The bulk wave shown in Fig. 3 is not visible on the particular scale.

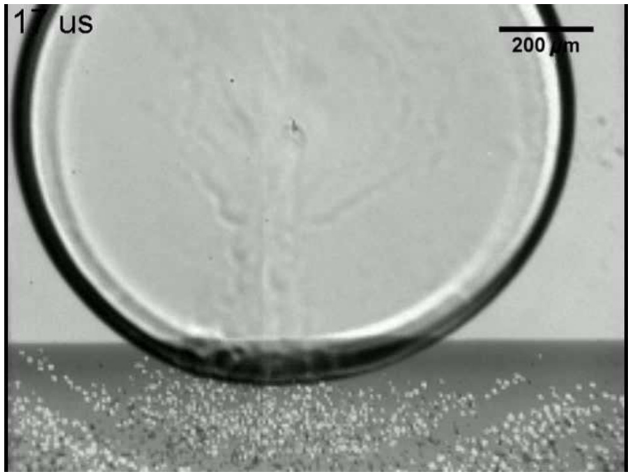

VIDEO 3. Recording showing the removal of a thin paint layer after nucleation of the secondary cavitation cloud. Thereafter the paint particles are transported by the liquid flow induced by the primary cavitation bubble. Selected frames are shown in Fig. 12.

[1] L. A. Crum, Tensile strength of water, Nature **278**, 148 (1979).

[2] A. A. Atchley, L. Frizzell, R. Apfel, C. Holland, S. Madanshetty, and R. Roy, Thresholds for cavitation produced in water by pulsed ultrasound, Ultrasonics **26**, 280 (1988).

[3] D. D. Joseph, Cavitation and the state of stress in a flowing liquid, J. Fluid Mech. **366**, 367 (1998).

[4] B. M. Borkent, S. Gekle, A. Prosperetti, and D. Lohse, Nucleation threshold and deactivation mechanisms of nanoscopic cavitation nuclei, Phys. Fluids **21**, 102003 (2009).

[5] M. E. M. Azouzi, C. Ramboz, J.-F. Lenain, and F. Caupin, A coherent picture of water at extreme negative pressure, Nat. Phys. **9**, 38 (2013).

[6] M. Blander and J. L. Katz, Bubble nucleation in liquids, AIChE J. **21**, 833 (1975).

[7] C. E. Brennen, *Cavitation and Bubble Dynamics* (Cambridge University Press, New-York, 2014).

[8] E. Herbert, S. Balibar, and F. Caupin, Cavitation pressure in water, Phys. Rev. E **74**, 041603 (2006).

[9] Q. Zheng, D. Durben, G. Wolf, and C. Angell, Liquids at large negative pressures: Water at the homogeneous nucleation limit, Science **254**, 829 (1991).

[10] F. Caupin and E. Herbert, Cavitation in water: A review, C. R. Phys. **7**, 1000 (2006).

[11] M. Frenz, G. Paltauf, and H. Schmidt-Kloiber, Laser-Generated Cavitation in Absorbing Liquid Induced by Acoustic Diffraction, Phys. Rev. Lett. **76**, 3546 (1996).

[12] H. W. Baac, J. G. Ok, A. Maxwell, K.-T. Lee, Y.-C. Chen, A. J. Hart, Z. Xu, E. Yoon, and L. Guo, Carbon-nanotube optoacoustic lens for focused ultrasound generation and high-precision targeted therapy, Sci. Rep. **2**, 989 (2012).

[13] K. Ando, A.-Q. Liu, and C.-D. Ohl, Homogeneous Nucleation in Water in Microfluidic Channels, Phys. Rev. Lett. **109**, 044501 (2012).

[14] P. A. Quinto-Su and K. Ando, Nucleating bubble clouds with a pair of laser-induced shocks and bubbles, J. Fluid Mech. **733**, R3 (2013).

[15] C. A. Stan *et al.*, Liquid explosions induced by X-ray laser pulses, Nat. Phys. **12**, 966 (2016).

[16] D. Veysset, U. Gutiérrez-Hernández, L. Dresselhaus-Cooper, F. De Colle, S. Kooi, K. A. Nelson, P. A. Quinto-Su, and T. Pezeril, Single-bubble and multibubble cavitation in water triggered by laser-driven focusing shock waves, Phys. Rev. E **97**, 053112 (2018).

[17] A. Salleo, S. T. Taylor, M. C. Martin, W. R. Panero, R. Jeanloz, T. Sands, and F. Y. Génin, Laser-driven formation of a high-pressure phase in amorphous silica, Nat. Mater. **2**, 796 (2003).

[18] R. Jeanloz, P. M. Celliers, G. W. Collins, J. H. Eggert, K. K. Lee, R. S. McWilliams, S. Brygoo, and P. Loubeyre, Achieving high-density states through shock-wave loading of precompressed samples, Proc. Nat. Acad. Sci. **104**, 9172 (2007).

[19] S. Juodkazis, K. Nishimura, S. Tanaka, H. Misawa, E. G. Gamaly, B. Luther-Davies, L. Hallo, P. Nicolai, and V. T. Tikhonchuk, Laser-Induced Microexplosion Confined in the Bulk of a Sapphire Crystal: Evidence of Multimegabar Pressures, Phys. Rev. Lett. **96**, 166101 (2006).

[20] C. J. Pickard and R. Needs, Aluminium at terapascal pressures, Nat. Mater. **9**, 624 (2010).

[21] D. Milathianaki, S. Boutet, G. Williams, A. Higginbotham, D. Ratner, A. Gleason, M. Messerschmidt, M. M. Seibert, D. Swift, and P. Hering *et al.*, Femtosecond visualization of lattice dynamics in shock-compressed matter, Science **342**, 220 (2013).

[22] C. B. Scruby and L. E. Drain, *Laser Ultrasonics Techniques and Applications* (CRC Press, Bristol, 1990), p. 223.

[23] C.-D. Ohl, O. Lindau, and W. Lauterborn, Luminescence from Spherically and Aspherically Collapsing Laser Induced Bubbles, Phys. Rev. Lett. **80**, 393 (1998).

[24] P. A. Quinto-Su, X. H. Huang, S. R. Gonzalez-Avila, T. Wu, and C.-D. Ohl, Manipulation and Microrheology of Carbon Nanotubes with Laser-Induced Cavitation Bubbles, Phys. Rev. Lett. **104**, 014501 (2010).

[25] J. Rapet, Y. Tagawa, and C.-D. Ohl, Shear-wave generation from cavitation in soft solids, Appl. Phys. Lett **114**, 123702 (2019).

[26] A. Vogel, S. Busch, and U. Parlitz, Shock wave emission and cavitation bubble generation by picosecond and nanosecond optical breakdown in water, J. Acoust. Soc. Am. **100**, 148 (1996).

[27] D. Devaux, R. Fabbro, L. Tollier, and E. Bartnicki, Generation of shock waves by laser-induced plasma in confined geometry, J. Appl. Phys. **74**, 2268 (1993).

[28] L. Chase, in *Laser Ablation* (Springer, Berlin, 1994).

[29] While the plasma is generated for the duration of the laser pulse (10 ns), its radiation during the recombination process lasts for about 100 ns as depicted in Fig. 4. This results in saturation on the pixels of the camera lasting a few frames in Fig. 2. This overexposure leads to two artifacts: a brighter area at $t = 1$ and 2μs in Fig. 2 and two differently shaded regions.

[30] O. Lindau and W. Lauterborn, Cinematographic observation of the collapse and rebound of a laser-produced cavitation bubble near a wall, J. Fluid Mech. **479**, 327 (2003).

[31] Y. Tagawa, S. Yamamoto, K. Hayasaka, and M. Kameda, On pressure impulse of a laser-induced underwater shock wave, J. Fluid Mech. **808**, 5 (2016).

[32] J. Zhu, J. S. Popovics, and F. Schubert, Leaky rayleigh and scholte waves at the fluid–solid interface subjected to transient point loading, J. Acoust. Soc. Am. **116**, 2101 (2004).

[33] S. Xiong, L. Chin, K. Ando, T. Tandiono, A. Liu, and C. Ohl, Droplet generation via a single bubble transformation in a nanofluidic channel, Lab. Chip. **15**, 1451 (2015).

[34] G. Menzl, M. A. Gonzalez, P. Geiger, F. Caupin, J. L. F. Abascal, C. Valeriani, and C. Dellago, Molecular mechanism for cavitation in water under tension, Proc. Nat. Acad. Sci. **113**, 13582 (2016).

[35] J. Achenbach, *Wave Propagation in Elastic Solids* (Elsevier, Amsterdam, 2012).

[36] A. Doinikov, F. Mekki-Berrada, P. Thibault, and P. Marmottant, Lamb-type waves generated by a cylindrical bubble oscillating between two planar elastic walls, Proc. R. Soc. A **472**, 20160031 (2016).

[37] H. Lamb, On waves in an elastic plate, Proc. Roy. Soc. A-Math. Phys. **93**, 114 (1917).

[38] M. W. Ewing, *Elastic Waves in Layered Media*, Tech. Rep. (McGraw-Hill, 1957).

[39] V. Aubert, R. Wunenburger, T. Valier-Brasier, D. Rabaud, J.-P. Kleman, and C. Poulain, A simple acoustofluidic chip for microscale manipulation using evanescent scholte waves, Lab. Chip. **16**, 2532 (2016).

[40] M. Dular and A. Osterman, Pit clustering in cavitation erosion, Wear **265**, 811 (2008).

[41] H. Soyama, Key factors and applications of cavitation peening, Int. J. Peening Sci. Tech. **1**, 3 (2017).

[42] C.-D. Ohl, M. Arora, R. Dijkink, V. Janve, and D. Lohse, Surface cleaning from laser-induced cavitation bubbles, Appl. Phys. Lett **89**, 074102 (2006).

[43] B. Verhaagen and D. F. Rivas, Measuring cavitation and its cleaning effect, Ultrason. Sonochem. **29**, 619 (2016).

[44] N. Vyas, K. Manmi, Q. Wang, A. J. Jadhav, M. Barigou, R. L. Sammons, S. A. Kuehne, and A. D. Walmsley, Which parameters affect biofilm removal with acoustic cavitation? a review, Ultrasound Med. Biol. **45**, 1044 (2019).

[45] C. Cairós and R. Mettin, Simultaneous High-Speed Recording of Sonoluminescence and Bubble Dynamics in Multibubble Fields, Phys. Rev. Lett. **118**, 064301 (2017).

[46] E. Zwaan, S. Le Gac, K. Tsuji, and C.-D. Ohl, Controlled Cavitation in Microfluidic Systems, Phys. Rev. Lett. **98**, 254501 (2007).

[47] A. N. Hellman, K. R. Rau, H. H. Yoon, S. Bae, J. F. Palmer, K. S. Phillips, N. L. Allbritton, and V. Venugopalan, Laser-induced mixing in microfluidic channels, Anal. Chem. **79**, 4484 (2007).

[48] T.-H. Wu, L. Gao, Y. Chen, K. Wei, and P.-Y. Chiou, Pulsed laser triggered high speed microfluidic switch, Appl. Phys. Lett. **93**, 144102 (2008).

[49] G. N. Sankin, F. Yuan, and P. Zhong, Pulsating Tandem Microbubble for Localized and Directional Single-Cell Membrane Poration, Phys. Rev. Lett. **105**, 078101 (2010).

[50] P. A. Quinto-Su, C. Kuss, P. R. Preiser, and C.-D. Ohl, Red blood cell rheology using single controlled laser-induced cavitation bubbles, Lab. Chip. **11**, 672 (2011).

[51] P. A. Quinto-Su, H.-H. Lai, H. H. Yoon, C. E. Sims, N. L. Allbritton, and V. Venugopalan, Examination of laser microbeam cell lysis in a pdms microfluidic channel using time-resolved imaging, Lab. Chip. **8**, 408 (2008).